Chapter 13
Tailoring of Hysteresis Across Different Material Scales

Walter Lacarbonara, Michela Talò, Biagio Carboni and Giulia Lanzara

Abstract Hysteresis is discussed as a multi-scale material feature that can strongly affect the dynamic performance of a structure. It is shown that the hysteresis exhibited by assemblies of short wire ropes can be tailored via a synergistic use of different dissipation mechanisms (inter-wire frictional sliding, phase transformations) combined with geometric nonlinearities. The blend of material and geometric nonlinearities is a powerful and promising way to design new advantageous types of hysteretic responses in macro- or micro-scale devices and structures. Indeed, moving from macro-scale structures towards much smaller material scales, carbon nanotubes in nanocomposites are shown to dissipate energy through stick-slip with the polymer chains. The hysteresis of these materials can be largely modified and optimized by adjusting the micro-structural constitutive features. Recent experimental and modeling efforts are discussed in the context of new directions in material design and dynamic behavior of nanocomposites.

13.1 Introduction

A large variety of natural or engineered materials and systems exhibit hysteresis through the looping behavior of the input-output response functions [1]. The macroscopically observed hysteresis is often the result of a combination of complex multi-scale interactions between parts of structural dynamic systems, or it may arise in the material itself. Hysteresis can be caused by local plastic deformations due to internal slippage within the crystalline lattice microstructure of metals, alloys, reticular

W. Lacarbonara (✉) · M. Talò · B. Carboni
Department of Structural and Geotechnical Engineering, Sapienza University of Rome, Via Eudossiana 18, 00184 Rome, Italy
e-mail: walter.lacarbonara@uniroma1.it

G. Lanzara
Department of Engineering, University of RomeTre, Via Vito Volterra 62, 00146 Rome, Italy
e-mail: giulia.lanzara@uniroma3.it

M. Belhaq (ed.), *Recent Trends in Applied Nonlinear Mechanics and Physics*,
Springer Proceedings in Physics 199, https://doi.org/10.1007/978-3-319-63937-6_13

polymers or due to phase transformations in shape memory alloys such as NiTiNOL (Nickel-Titanium Naval Ordnance Laboratory). Often hysteresis is due to friction damping as observed in gears, joints, wire ropes or granular materials. Hysteresis can also result from micro-nano slippage between two or more phases of a composite material or a multifunctional, multi-phase material. Thus, we can define hysteresis as a macroscopically observed phenomenon featured at different material scales.

This fascinating phenomenon is here discussed extensively ranging from the macroscale to the nanoscale to show how the distinct properties of hysteresis can be tailored and engineered towards innovative designs and applications dealing with wire ropes and carbon nanotube nanocomposites.

Wire ropes are load-bearing members which are largely employed in applications requiring the lift of huge masses or the support of long-span decks such as in suspension bridges [2]. Short wire ropes subject to bending or coupled tension-bending can dissipate large amounts of energy through the inter-wire friction developing through the wire-to-wire and rope-to-rope contact areas which, in turn, depend on the shear, longitudinal, and radial stress components. This property makes wire ropes perfect rheological elements in applications requiring restoring forces which provide at the same time stiffness and damping. Recent patents addressed nonlinear hysteretic devices mainly conceived for vibration control purposes [3, 4]. The device of Lacarbonara and Carboni [4] exploits the stiffness and energy dissipation provided by an assembly of hybrid wire ropes made of AISI steel wires and NiTiNOL wires. The energy dissipation is due to the concurrency of inter-wire friction and NiTiNOL phase transformations [5]. The combination of these dissipation mechanisms with the stretching-induced geometric nonlinearity gives rise to the possibility of tailoring the restoring force and the associated hysteresis shape for different applications. In the present chapter, the role of dissipation mechanisms and geometric nonlinearities in the design of an optimized hysteretic response is elucidated. Moreover, the proper modeling tools adopted for the mathematical description of the physical nonlinearity are also discussed. In particular, the results of a finite element computation are discussed to justify the adoption of phenomenological approaches towards wire ropes mechanics and related design problems.

Another interesting class of lightweight materials exhibiting hysteresis shapes is the class of nanostructured polymer composites featuring different kinds of filler in the form of 0D nanoparticles (e.g., silica, nano-oxides and other inorganic particles), 1D nanofibers (e.g., carbon nanotubes, collagen nanofibers, and other nanofibers), and 2D nanolayers (e.g., nanoclay, graphite, graphene, layered silicate). Nanocomposite materials offer the potential for unprecedented improvements in stiffness, toughness, strength, damping and more general multifunctional aspects, without incurring weight penalty [6–12]. The integration of a strong filler into a polymeric hosting matrix is usually dictated by reinforcement purposes. On the other hand, in the last decades, experimental results have shown the potential of several micro- to nano-scale fillers to enhance not only the mechanical properties but also the damping capacity. In nanocmposites, damping mainly arises from the interfacial slippage between the filler and the surrounding matrix [13].

Such interfacial slippage primarily depends on the interfacial shear strength (i.e., the shear stress limit at which the sliding motion is activated at the interfaces). The resulting hysteresis in the stress-strain cycles becomes increasingly larger with an increasing interfacial contact area between the two constituents as is also the case at the macro scale with wire ropes where the amount of dissipation depends on the amount of inter-wire contact area. When the size of the filler approaches the nanometer scale as is the case with carbon nanotubes, for a given volume fraction of the filler, the composite macroscopic hysteretic response becomes more important. Indeed, the nanometer size of the filler is capable of providing a huge specific interfacial surface area through which shear slippage may occur, thus, giving rise to a higher energy absorption capability. Nanofillers have the virtue of modifying and enhancing the hysteresis and strength of the hosting matrices. The main factors affecting the damping capacity of the nanocomposites include the nanofiller aspect ratio, the volume fraction and dispersion, the nature of the interaction forces between the nanofiller and the matrix, as well as the employed manufacturing process [9].

Among all existing nanofillers, carbon nanotubes (CNT) offer the highest ratio between interfacial area and volume fraction. Indeed CNTs exhibit a hollow cylindrical structure with a diameter of a few nanometers and a length ranging from 1 μm to 1 mm thus giving rise to high aspect ratios (L/D). The literature confirmed that CNTs are the most promising candidate fillers to improve the damping capability of polymers even with very low CNT weight fractions [10, 11]. CNTs are known for their excellent elastic properties since the Young modulus can be as high as 1 TPa and the predicted tensile strength can be as high as 100 GPa [12]. However, to exploit their mechanical properties several manufacturing challenges must still be overcome. The interaction forces between CNTs and the surrounding polymer chains are mostly represented by weak van der Waals forces, which can be overcome even when the material is subject to low strains in the elastic region of the hosting matrix. A weak adhesion between the nanotubes and the matrix is the key for the activation of the frictional sliding motion called stick-slip [13, 14], which has the advantage of being reversible in a given range of strain amplitudes. Provided that the fabrication challenges are overcome, compared to other nanofillers, carbon nanotubes can enable a wider tuning of the mechanical and hysteretic properties of the nanocomposites response opening up a wide range of opportunities for the use of strong and highly damped composites [15–20].

Understanding the relationships between the nanocomposites microstructural properties and the macroscopic hysteretic response will pave the way towards unprecedented optimization of the nonlinear material behavior of new composite materials. This chapter will first discuss the hysteresis of wire rope assemblies and its application in the field of vibration absorption and proceed with discussing hysteresis observed in various carbon nanotube nanocomposites under the prevailing loading conditions.

13.2 Hysteresis in Wire Ropes

Wire ropes can be classified according to their cross-sectional geometry resulting from the formation process. There are spiroidal and stranded wire ropes. The first are characterized by an individual strand with a central core wire and a certain number of layers of wires wrapped around. The second type is represented by multiple strands which are wrapped around a central core strand. In principle, an infinite variety of wire ropes can be obtained varying the number, diameter, laying direction of the wires or strands. According to these features the contact area between the wires can be augmented or reduced implying different levels of energy dissipation when the resulting wire ropes are subject to cyclic loads.

The materials constituting the wires play an important role. The material can be elastic, elasto-plastic, pseudo-elastic, etc. For example, the introduction of shape memory alloy wires in combination with classical steel wires entails significant changes in the dissipative features of the ensuing wire ropes [5]. A shape memory alloy, according to its chemical composition, can exhibit material behaviors known as shape recovery effect and pseudo-elasticity.

These properties can be activated varying the thermal state or the stress state of the material. Herein, we will focus on the pseudo-elastic effect observed when the material is subject to a cyclic loading program.

Experimentally observed hysteresis. Figure 13.1 shows the tensile tests performed on an individual NiTiNOL wire, a 7-wire NiTiNOL strand and a mixed NiTiNOL-steel spiroidal wire rope. The force-strain curve for the NiTiNOL wire (see Fig. 13.1a) shows the pseudo-elastic effect typically observed in shape memory alloys. When the load is removed there are no residual strains thanks to the particular crystalline structure of the material. However, at the end of the cycle, a certain amount of energy, given by the area enclosed in the hysteresis loop, is dissipated. On the other hand, the 7-wire NiTiNOL strand in Fig. 13.1b exhibits a small residual strain after unloading. This is due to the frictional sliding between the wires. For the hybrid spiroidal wire rope, the large contact area between the wires provides a large frictional dissipation that is reflected on the residual strain at zero tension. Moreover, the changes in slope along the loading and unloading branches are due to the phase transformations of the shape memory material.

As mentioned, the dissipation occurring in a wire rope is mainly due to inter-wire sliding and its level depends on the normal contact forces between the wires. The literature about wire rope mechanics classifies the contact modes between lateral and radial contact [21]. The lateral or circumferential contact occurs between the wires of the same layer. The associated contact surfaces have a continuous helical shape across the rope length. This type of contact is strongly affected by the manufacturing process and the wear level. Radial contact occurs between the different layers through contact surfaces presenting discontinuous helical shapes across the rope length. These contact modes refer to spiroidal wire ropes but are generally valid also for multiple stranded wire ropes. The hysteresis provided by a wire rope can be selectively modified by

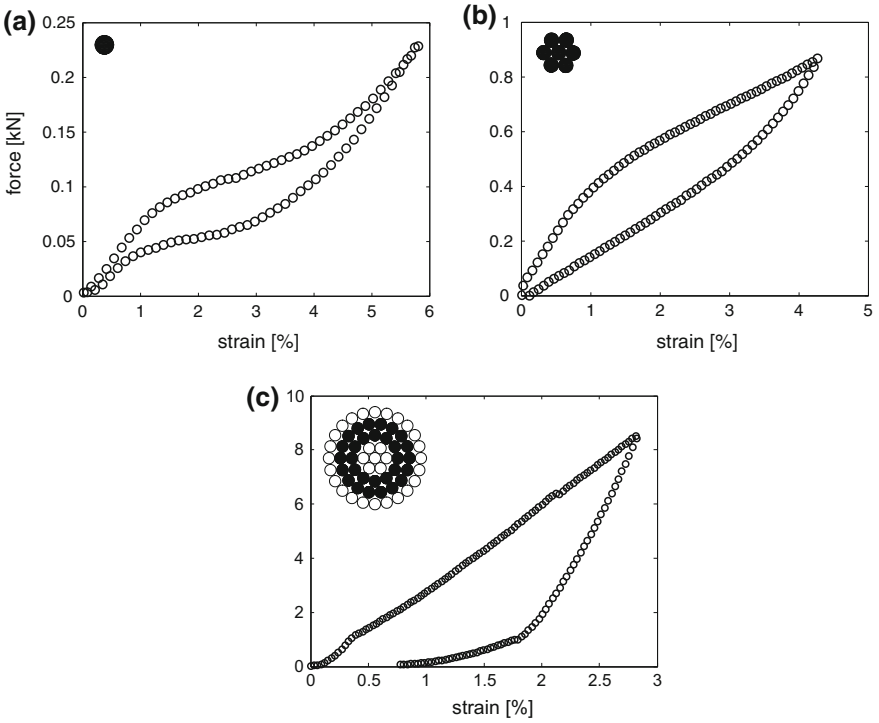

Fig. 13.1 Experimental stress-strain curves obtained via uni-axial tensile tests for **a** an individual NiTiNOL wire with $D = 0.63$ mm, **b** a 7-wire NiTiNOL strand with $D = 1.8$ mm and **c** a mixed spiroidal NiTiNOL steel wire rope with $D = 5.7$ mm. The *black* (*white*) *color* indicates that the wire is made of NiTiNOL (steel)

acting on the internal contact properties and regulating the geometrical wire rope parameters.

The hysteretic response depends also on the loading condition and on the activation of the geometric nonlinear hardening effect. The shape of the hysteresis loops can be regulated combining different types of wire ropes and stress states such as pure bending or coupled tension-bending.

Figure 13.2e, f show the testing setups employed to acquire the restoring forces exhibited by different wire ropes subject to cyclic displacements. These setups are custom made and make use of a linear actuator. The testing setups shown in Fig. 13.2e, f are mounted on the Material Testing System (MTS) available in the Materials and Structures Laboratory at Sapienza University of Rome. One end of the wire rope is vertically displaced while the other end is connected to a load cell that measures the restoring force. Different stress conditions can be implemented according to the horizontal restraint applied to the wire ropes. When a vertical displacement is prescribed, the deflected end of the wire ropes can be free or prevented to slide along the horizontal direction. In the first case the wire rope is subject to pure bending

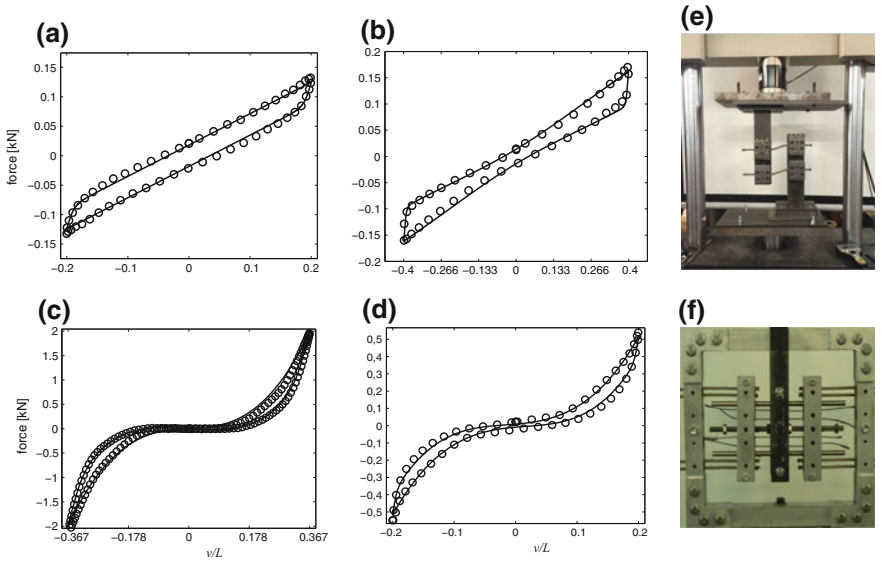

Fig. 13.2 Experimental response curves (*circles*) together with the identified curves (*solid lines*): **a** 8 steel multi-stranded wire ropes with $D = 6$ mm and $L = 100$ mm; **b** 4 mixed NiTiNOL-steel spiral wire ropes with $D = 5.7$ mm and $L = 75$ mm; **c** 8 NiTiNOL 7-wire stranded ropes subject to bending and tension with $D = 1.8$ mm and $L = 56$ mm; **d** 8 steel multi-stranded ropes with $D = 1.8$ mm and $L = 100$ mm subject to bending and tension with 2 additional horizontal NiTiNOL 7-wire strands with $D = 1.8$ mm and $L = 63$ mm. Experimental setups for testing wire ropes assemblies under **e** Bending or tension-bending and **f** With the additional horizontal stiffness provided by secondary wire ropes

states while in the second case the rope is stretched exhibiting a nonlinear geometric stiffness effect of the hardening type. An intermediate stress condition can be implemented introducing an additional horizontal restoring force provided by springs or secondary wire ropes. This testing condition is obtained with the setup shown in Fig. 13.2f. A detailed description of this testing device is given in [5, 22]. The hysteresis loops obtained with different wire rope types and working conditions are shown in Fig. 13.2a–d. Part (a) portrays the hysteresis cycle of steel wire ropes subject to bending. Part (b) shows the hysteretic force of mixed NiTiNOL-steel wire ropes subject to bending. The interaction between friction and phase transformations is revealed by the pinched loop around the origin. When the shape memory material is unloaded and it goes back to the austenitic phase, the return on the elastic branch determines a pinching in the restoring force. Part (c) shows a strong pinching at the origin of the force-displacement cycle and a distinct hardening behavior. This behavior is due to the generated tensile forces in the ropes as a consequence of the horizontal constraint. Part (d) shows a slightly pinched, hardening hysteresis due to NiTiNOL strands subject to coupled bending-tensile loads. The force-displacement cycle in part (d) is obtained introducing the additional horizontal restoring force due

to axially stretched NiTiNOL wires that introduce an additional source of energy dissipation.

Modeling and identification. A fine mechanical modeling of wire ropes is a challenging task mainly because of the large number of wires interacting through contact surfaces with complex geometry. While 3D finite element discretizations can certainly incorporate fine details of the actual geometry and suitably describe inter-wire frictional forces, such a computational approach is very demanding.

By employing Abaqus [23], a steel 19-wires $(1 + 6 + 12)$ strand of diameter $D = 3$ mm and length $L = 65$ mm was discretized into about 3×10^5 8-node tetrahedral elements with linear shape functions. Forward time integrations of the nonlinear equations of motion were performed and a penalty formulation was adopted for the normal and tangential contact problem between the wires. Figure 13.3a shows the finite element model in the undeformed configuration. Each wire end at the root cross section is clamped while the other ends are subject to a transverse displacement time history described by $v(t) = A_1 \sin 2\pi f_1 t$ where $A_1 = 10$ mm, $f_1 = 3.33$ Hz and $t \in [0, 0.3]$ s. The displaced ends are torsionally constrained and kept at the same distance L from the root. In a first set of simulations, the wire rope is initially stress-free while, in the second set, the rope is given an initial pretension through a prescribed longitudinal displacement monotonically increasing up to 0.8 mm. Figure 13.3b shows the contact stresses between the wires while Fig. 13.3c, d depict the total reaction force at the clamp along the transverse direction and the time change of inter-wire contact area for the initially stress-free rope. Figure 13.3e, f describe the force and contact area for the pre-stressed rope.

The hysteresis curve in Fig. 13.3c shows a very pronounced pinching at the origin indicating a low dissipation rate when the strand is unloaded. It is due to the weak contact stresses which are proportional to the axial force in the strand. When the transverse deflection is increased, tension arises in the wires determining a global hardening response together with an increment of the contact forces which in turn gives rise to larger energy dissipation. The same behavior was observed experimentally in Fig. 13.2c [5, 22, 24]. When the wire rope is given a pre-tension, the pinching is negligible and the hystersis loop becomes fatter indicating a greater dissipation due to the larger contact area through which frictional sliding produces dissipation.

The computational time of the Abaqus finite element model exceeds 24 h employing a desktop computer. The heavy computational burden does not allow to use this approach for identification or optimisation purposes. This reason justifies the adoption of much lighter phenomenological models or reduced order models. Indeed phenomenological models can be effectively employed to fit the experimental force-displacement curves by using parameters identification methods such as the Differential Evolution Algorithm [25] or other data-driven strategies [26]. The well-known Bouc-Wen hysteretic model [27, 28] was modified in [5] to describe the pinching at the origin of the force-displacement cycles. The restoring force f depends on the displacement x according to

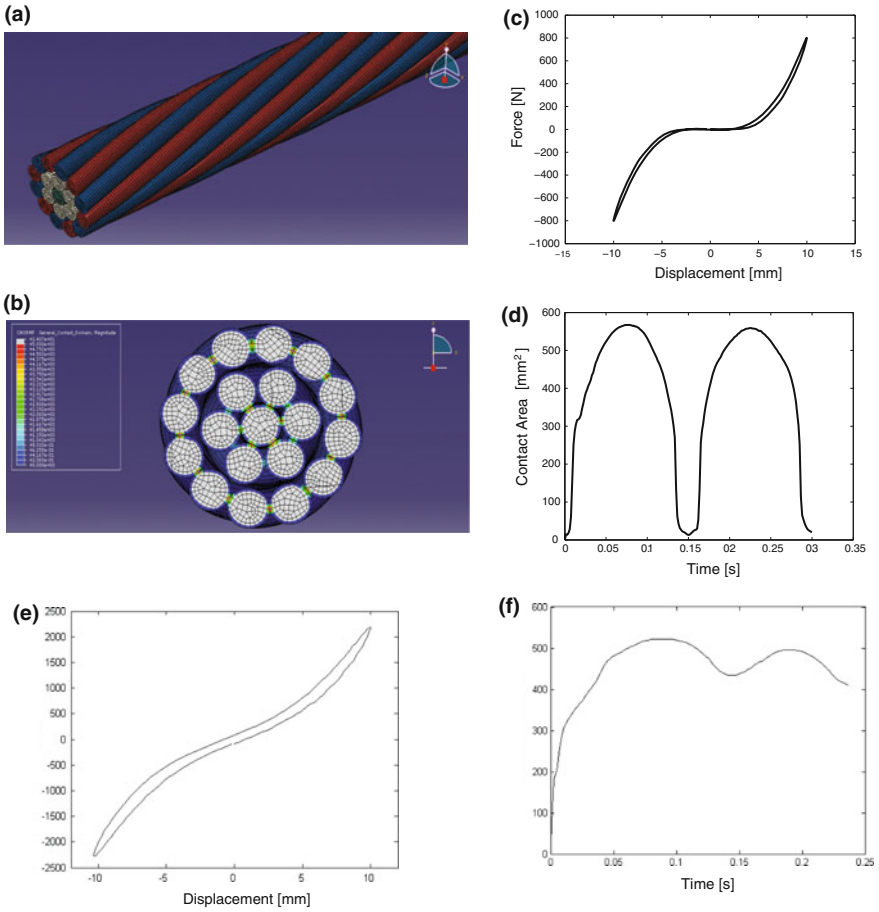

Fig. 13.3 Finite element model of a 19-wire steel strand: **a** Reference configuration; **b** Contour plot of the inter-wire normal contact forces; **c** and **e** Force-displacement cycles of (**c**) stress-free rope and **e** Pre-stressed rope; **d** and **f** Variations with time of the contact area of (**d**) stress-free rope and **f** Pre-stressed rope. The material parameters are: Young's modulus $E = 206$ GPa, Poisson's coefficient $\nu = 0.3$, frictional coefficient $\mu = 0.5$

$$f = k_e x + k_3 x^3 + z, \qquad \dot{z} = \left[k_d h(x) - (\gamma + \beta \text{sgn}(\dot{x} z)\, |z|^n\right] \dot{x} \tag{13.1}$$

where k_e and k_3 represent the elastic linear and cubic stiffness coefficients, respectively, and z is the hysteretic part of the force. The overdot denotes differentiation with respect to time t and (k_d, γ, β, n) are the model parameters regulating the hysteresis loops shape. When $k_3 = 0$, the stiffness at the origin of the cycles is $k_e + k_d$ while past a threshold force the stiffness reaches the plateau value equal to k_e. The pinching function $h(x)$ is given by $h(x) = 1 - \xi \exp(-x^2/x_c)$ with $\xi \in [0, 1)$ regulating the pinching severity and $x_c > 0$ defining the extension of the pinching zone along the

displacement axis. The hysteretic responses shown in Fig. 13.2a–d are accurately identified using (13.1) as shown by the closeness of the solid lines to the experimental measurements. The cubic stiffness k_3 was set to zero for identifying the cycles in Fig. 13.2a, b. Moreover, the pinching function $h(x)$ was set to 1 in Fig. 13.2a. A clear interpretation of the role of each parameter is given in [5, 22].

A good compromise between expensive 3D FE models and phenomenological models is the one-dimensional reduction of a wire rope to a nonlinear hysteretic geometrically exact cylindrical beam model [29]. The generalized hysteretic constitutive relationship was established between the bending moment and the beam curvature within the special Cosserat theory of shearable beams. This approach provides the hysteretic response as well as the internal resultant stresses in the wire rope.

The shape of the restoring forces can be largely varied regulating the geometric and mechanical features. For example, it is possible to change the cross section and material properties of the wire ropes, their number, length, and diameter. Moreover, the presented device [4] allows to tune the geometric nonlinearities and stiffness ratio between the different wire rope components so as to vary the loop shapes.

Hysteretic damping capacity. The damping capacity associated with the obtained constitutive behaviors can be measured by the so-called equivalent damping ratio expressed as

$$\xi_0 = \frac{W_D}{4\pi W_E} \tag{13.2}$$

where W_D denotes the energy dissipated in a loading-unloading cycle and is given by the area enclosed by the force-displacement cycle. W_E indicates the elastic energy stored in an equivalent visco-elastic rope at the end of the loading branch. The evaluation of the stored energy is not unique since it depends on the assumed elastic stiffness of the system. The equivalent damping ratio is meaningful if an equivalent visco-elastic rope (comparison system) is found with a stiffness leading to the same oscillation frequency of the actual hysteretic rope at a given oscillation amplitude. Such stiffness can be set to be the secant stiffness or some other average stiffness over the considered displacement cycle. Figure 13.4 shows the equivalent damping associated with the different constitutive behaviors. All damping curves show a peak at moderately low displacement amplitudes. Thereafter the curves roll off at different rates due to the different evolutions of inter-wire friction and phase transformations at high oscillation amplitudes.

13.2.1 Tailoring the Wire Ropes Damping in Hysteretic Vibration Absorbers

The device proposed in [4] exploits the richness of hysteretic behaviors obtained combining different wire rope assemblies. Such device can be employed as a Tuned

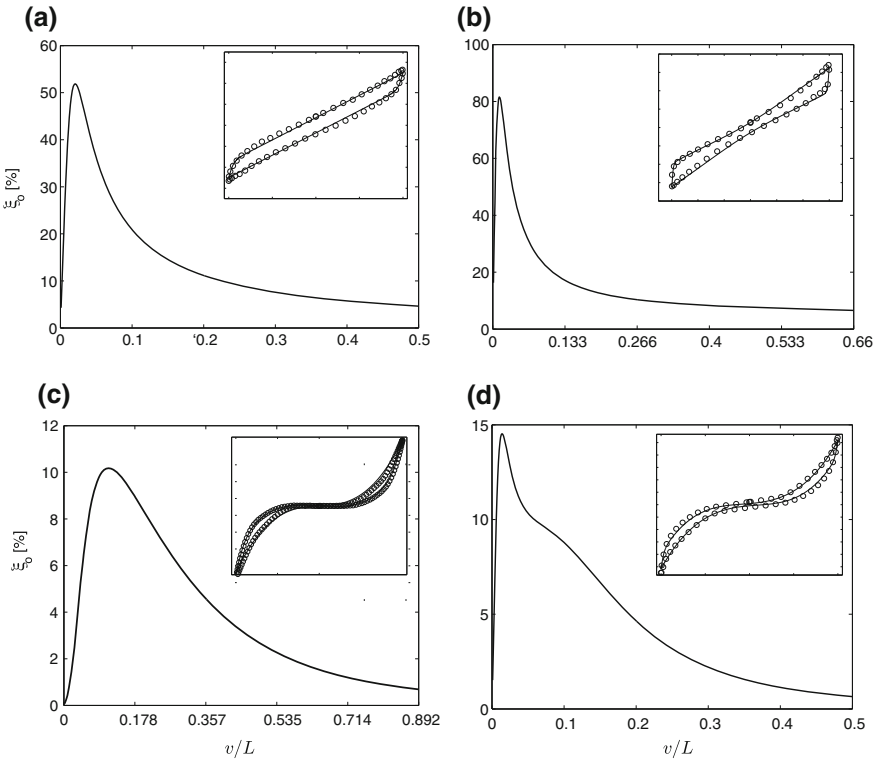

Fig. 13.4 Equivalent damping versus displacement amplitude. The damping curves in parts **a**, **b**, **c** and **d** are referred to the constitutive behaviors shown in Fig. 13.2, respectively

Mass Damper (TMD) for vibration mitigation of structures subject to base motions or direct excitations.

A hysteretic TMD [4] was experimentally investigated in [24] for vibration control of a scaled multi-story building subject to harmonic base excitation. The stiffness and damping of the absorber were tailored to achieve optimal control of the fundamental sway mode of the building. The low-frequency sway modes of a building usually exhibit a linear behavior. In the literature, it is commonly accepted that the optimal stiffness and damping of a TMD designed for mitigating harmonic motions of viscously damped structures must be independent of the displacement amplitude. Many authors provided analytical or empirical expressions to estimate the optimal TMD mechanical parameters [30–35].

The engineering forms according to which vibration absorbers have been realized in the literature comprise reinforced rubber bearings, pistons containing viscous liquids, metal springs in parallel with viscous dampers, devices based on the rolling or sliding friction. The stiffness and damping of these devices exhibit very different behaviors. Invariably, the fundamental drawback is represented by the difficulty of

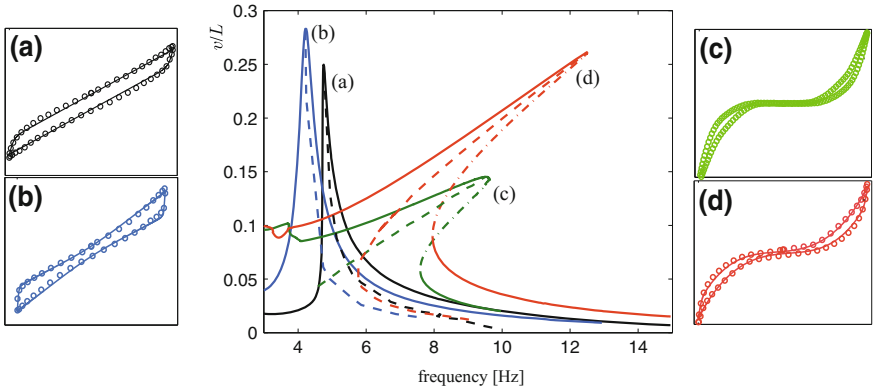

Fig. 13.5 **a** Requency-response curves at various excitation levels for absorbers exhibiting the hysteretic restoring forces labelled (**a**), (**b**), (**c**), (**d**). The *solid* and *dashed-dotted lines* denote the stable and unstable responses, respectively, while the *dashed lines* represent the associated backbone curves

obtaining restoring forces which maintain a constant stiffness and constant damping at large oscillation amplitudes typically attained by the TMD masses oscillating at resonance.

The hysteretic cycle shown in Fig. 13.2b has the peculiarity of providing a large-amplitude displacement range within which both stiffness and damping are nearly constant. This particular feature, as discussed in [24], ensures a good performance of the wire rope-based TMD for controlling the structure dynamics especially at large oscillation amplitudes.

Figure 13.5 shows the frequency-response curves of the different devices whose restoring forces are labelled (a), (b) (c) (d). The devices (a) and (b) exhibit pronounced softening while the devices (c) and (d) are characterized by strong hardening. Of particular interest is the restoring force in Fig. 13.2b. The increment of energy dissipation for increasing oscillation amplitudes due to the NiTiNOL phase transformations makes the ratio between dissipated and elastic energy almost constant. Moreover, the constant stiffness exhibited above a threshold displacement ensures that the resonance frequency also achieves an asymptotic constant value. The other important advantage of the proposed device consists in the fact that both stiffness and damping are provided by the wire ropes without the need of combining multiple rheological elements.

13.3 Hysteresis in Carbon Nanotube Nanocomposites

The hysteresis exhibited by short wire ropes results from a macroscopic frictional sliding between the individual wires. In this section we will discuss the hysteresis observed in nanocomposite materials for which the internal frictional dissipation

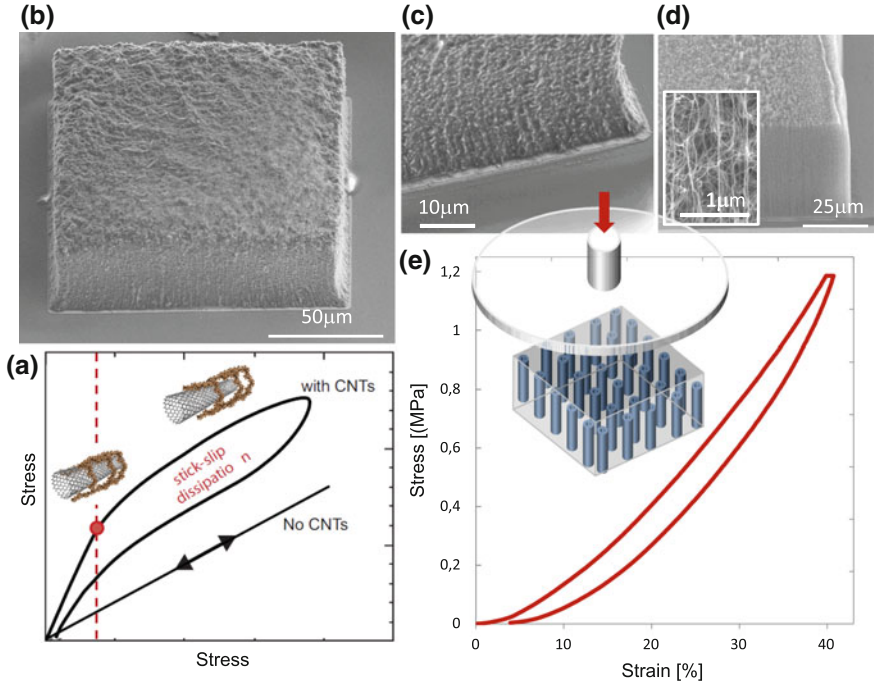

Fig. 13.6 **a** Schematic illustration of the stick-slip phenomenon; **b** CNT/PDMS nanocomposite micropattern; **c** Higher magnification of the nanocomposite; **d** Patterned oriented CNTs before absorption of the hosting matrix and a higher magnification of the same (see inset); **e** Schematic of the test setup and a compressional stress-strain curve

takes place at much smaller scales, namely, at the micro- and nano-scales through sliding between the hosting matrix and the CNTs when the interfacial shear stress reaches the limit value called interfacial shear strength (see Fig. 13.6). A nanocomposite micropillar made of PDMS and a high density array of oriented multi-walled carbon nanotubes (MWNT) was tested under compressional strain cycles in [36]. Forests of oriented MWNTs (35 μm thick) were first grown and patterned in microscaled square pillars (130 μm side) following the procedure described in [36, 37] (see Fig. 13.6d). A thin PDMS layer (Sylgard 182-Dow Corning) was absorbed within the micropillar forming the nanocomposite microstructure (20% CNTs volume fraction) [36, 38]. Figure 13.6b shows the nanocomposite micropillar, while Fig. 13.6c represents a higher magnification of the micropillar in which the good CNTs dispersion within the hosting PDMS matrix is highlighted. The embedded MWNTs are vertically oriented and highly packed (intertube spacing ranging from few nanometers to 250 nm). This is shown in Fig. 13.6d representing the CNTs micropattern before being impregnated with the matrix. Compression tests were performed with a nanoindentation technique using a nanoscratch tester in indentation mode (CSM Instruments). Micropillars were uniformly compressed by means of a flat tip

(2 mm diameter) as shown in Fig. 13.6e. A linear load up to 20 mN at a loading rate of 40 mN/min, reaching nearly 40% compressional strain, was applied to the micropillar and, after a pause of 20s, the sample was fully unloaded at the same speed. The material clearly showed a hysteretic response with a hardening effect during loading. The elastic modulus in the loading cycle was found to be at least one order of magnitude higher than those reported in the literature for pure PDMS samples cured at room temperature [39], and over two orders of magnitude higher in the unloading cycle that is considered to be purely elastic in nanoindentation tests. However, these comparisons are very difficult due to the wide dependence of the PDMS properties on the curing process [39], the ratio of the curing agent [40], the type of elastomer (Sylgard 182 or 184) and the size of the sample [41]. None of the cases reported in the literature corresponds to the presented sample type, size, testing methodology as well as fabrication process (which also includes the addition of solvents to thinner the layer during fabrication). Wide variations are also reported in terms of loading/unloading cycles both in tensile and compression modes. Most commonly a linear elastic response is highlighted up to strains of the order of 50% and a hysteretic response for even larger strains (see, e.g., [39, 40]). It is here observed that the integration of oriented CNTs in the matrix induces a hysteretic response at all strain levels (well below 50%). These loops show an overall wider area especially toward the end of the unloading cycle if compared with the trends reported for higher strains [40, 42]. This effect is certainly related to the oriented CNTs which first affect the PDMS chains distribution within the sample during fabrication, and then affect the overall viscoelastic response. The CNTs in the forest are in fact highly packed forming an array of nanochannels that absorb the polymer chains from the substrate hosting the CNTs micropattern, in agreement with the fabrication procedure. The polymer chains are forced to align along the nanochannels length. Thus, the material becomes a hybrid aggregation of long and aligned fibers (the PDMS chains and the CNTs) that can relatively slide when loaded.

A wider experimental campaign was carried out on macroscopic nanocomposite samples with randomly oriented CNTs. The nancomposite samples were fabricated according to the details given in [19]. A campaign of cyclic tensile and torsional tests was conducted in different testing conditions to investigate hysteresis and the associated damping capacity. Cyclic tensile tests were carried out at increasing strain amplitudes using a Zwick/Roell Universal Testing Machine. Specimen shapes, test speeds and methods were selected according to ISO 527-1 and -2. In particular, dog-bone type-5B nanocomposite specimens were chosen according to ISO 527-2 with an overall length equal to 50 mm, gage length equal to 12 mm, and cross section equal to 2×4 mm^2.

The first investigated macroscale nanocomposite is made of polypropylene (PP), a commodity viscoelastic, thermoplastic polymer with a Young modulus equal to 1.45 GPa. The employed MWNTs have a low aspect ratio (L/D = 155). Other investigated nanocomposites feature engineering polymers, namely, polycarbonate (PC) and polybutylene terephthalate (PBT), with high mechanical properties (E = 3.7 GPa for PBT) and good resistance to chemical agents and heat.

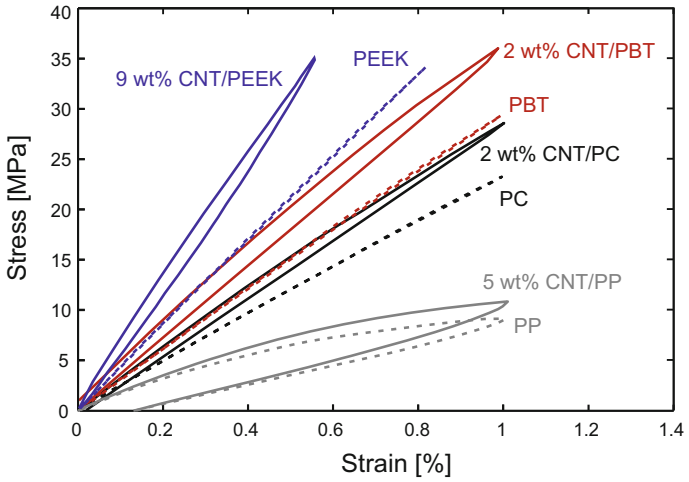

Fig. 13.7 Cyclic tensile tests on PP, PC and PBT nanocomposites showing the influence of different polymer matrices on the ensuing hysteresis loops. The cyclic tests are compared with the tests of Ogasawara et al. [43] carried out on PEEK nanocomposites

A first estimate of the nanocomposites damping capacity can be directly obtained through the tensile loading/unloading cycles. The energy dissipated per cycle W_D is measured as the area enclosed by the loop cycle, while the elastic energy stored in the material W_E is given by the area below the loading branch. Thus, the ratio W_D/W_E can be taken as a measure of the specific damping capacity of the material.

The role of the polymer matrix. Figure 13.7 shows the tensile stress-strain curves compared with the cyclic tests of a high-performance polyether ether ketone (PEEK) nanocomposite, previously investigated by Ogasawara et al. [43]. The shape of the hysteresis loops is controlled by the polymer matrix [44]. The cyclic curve of the PP nanocomposite shows a large enclosed area with a significant residual strain resulting from the pronounced viscous damping properties of the PP viscoelastic polymer, as confirmed by the residual viscous strain at the end of the cycle of the neat PP. On the other hand, the Young moduli of the engineering polymers referred to as PC, PBT and PEEK are higher than that of PP. The very narrow cycles obtained for PC, PBT and PEEK indicate the prevalence of the elastic energy component, since the cycles are mostly closed at the origin given the negligible residual strain at full unloading. For these engineering polymer nanocomposites, the damping capacity can be effectively associated with the internal hysteresis caused by the interfacial sliding motion between CNTs and polymer chains. Indeed, the interfacial shear stress needed to activate the stick-slip phenomenon is lower than the yielding stress in the high-performance polymers, as proved also for other PEEK nanocomposites [43, 45]. In addition, the damping capacity of the PP nanocomposite is not higher than that exhibited by the engineering thermoplastic nanocomposites. Although the area enclosed by the cycle in the CNT/PP nanocomposite appears to be larger compared

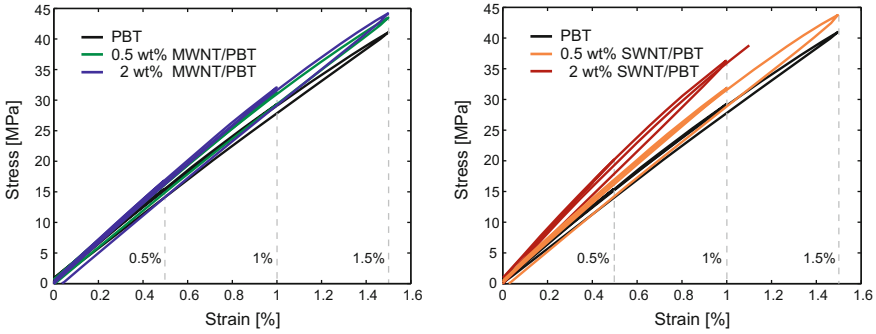

(a) Low aspect ratio MWNTs nanocomposites (b) High aspect ratio SWNTs nanocomposites

Fig. 13.8 Cyclic tensile tests conducted on pure PBT and CNT/PBT nanocomposites showing the influence of different aspect ratio nanofillers. The selected displacement rate was 2 mm/min by increasing the deformation of 0.5% at each loading process. The maximum reached deformation was 1.5% after three loading/unloading cycles

to that of the engineering nanocomposites, the actual damping increment provided by the addition of the CNTs is marginal with respect to the viscous damping component of pure PP. Moreover, the increment of dissipated energy is mainly due to the higher stiffness of the CNT/PP nanocomposite, as testified by the higher slope of the loading branch. This trend indicates that hysteresis observed in thermoplastic nanocomposites is considerably affected by the viscous behavior of the polymer, which may be predominant with respect to the CNT/matrix stick-slip effect. An interpretation of the phenomenon can be given by considering the PP polymer chains mobility and deformability. In soft matrices the polymer chains sliding is triggered by lower shear stresses compared to those needed to activate the stick-slip at the CNT/matrix interfaces. This behavior results in an augmentation of the dissipated energy per cycle, only because the elastic energy stored in the cycle is also increasing. Therefore, the nature of the hosting matrix plays a key role in tailoring the hysteresis of nanocomposite materials, mainly by dictating the shape of the loops.

CNT aspect ratio. The effects of the CNT aspect ratio were investigated in PC and PBT nanocomposites incorporating high aspect ratio single-walled nanotubes (SWNT) with L/D = 2778, in addition to the nanocomposites with low aspect ratio MWNTs (L/D = 155). In all nanocomposites with 0.5 and 2% CNT weight fractions (see Fig. 13.8) there is an increase of the specific damping capacity with respect to the neat polymer. The specific damping capacity increment for the intermediate cycle with 1% strain amplitude is found to be 47% with the addition of 0.5 wt% of MWNTs, and 64% with the addition of 0.5 wt% SWNTs. As expected, the nanocomposite dissipative and mechanical properties are strongly influenced by the CNT aspect ratio. High aspect ratio CNTs provide a larger interfacial area during the activation of the stick-slip phenomenon, thus, SWNT nanocomposites exhibit a more pronounced hysteretic behavior than composites with the lower aspect ratio MWNTs. The drawback of the employed long SWNTs is that good CNT dispersions

in the matrix are harder to pursue. The formation of CNT agglomerates causes stress concentrations. Thus nanocomposites with higher CNTs contents may undergo premature brittle failures, as observed for the 2 wt% SWNT/PBT nanocomposites.

CNT dispersion and functionalization. In addition to the considered thermoplastic nanocomposites, MWNT/epoxy composite samples (i.e., thermosetting matrix) were also tested to understand the influence of the CNT macro- and nano-dispersion on the material macroscopic response. Due to electrostatic and van der Waals attractive interaction forces between the CNTs themselves, they have a tendency to aggregate together. The aggregated CNTs are in the form of bundles or ropes usually with a highly entangled network structure that is difficult to disperse. The homogeneous dispersion of nanofillers within the polymer matrix is a prerequisite of any composite, that may be achieved through mechanical treatments such as shear mixing and ultrasonic dispersion techniques, sometimes combined with chemical treatments [46]. Chemical treatments may consist of (i) non-covalent functionalizations, which do not alter the CNT interface properties but require the use of chemical agents and surfactants to facilitate the CNT dispersion in the surrounding polymer matrix, and (ii) covalent functionalizations, which imply a modification of the chemical interaction forces between the CNTs and the polymer chains by exploiting functional molecules which strengthen the chemical bonds between these two constituents.

Cyclic tensile tests were performed for three epoxy nanocomposites with 0.5 wt% MWNTs content of (see Fig. 13.9). As observed in the light microscopy micrographs (see Fig. 13.9a), the CNT chemical treatment through amino-functionalization turned out to be the most effective treatment to achieve a good CNT dispersion and CNT/matrix adhesion, thus improving the nanocomposite macroscopic elastic response. However, the amino-functional groups strengthened the chemical bonds between the CNTs and epoxy, thus inhibiting or delaying the interfacial stick-slip activation. On the other hand, the effect of mechanical dispersion treatments—(i.e., a milder and a stronger ultrasonication via the ultrasonic bath and the ultrasonic horn, respectively—)led to a slightly improved mechanical response, but preserving and even enhancing the damping capacity. Indeed, the onset of stick-slip interfacial sliding in the non-functionalized nanocomposites occurs when the interfacial van der Waals forces are overcome.

Although various drawbacks may be introduced by the CNT functionalization processes (CNTs damage, shortening, etc.), the engineering of the CNT/matrix interfaces, as a whole, is regarded as a powerful technique to act on the local morphology of the nanotubes and tailor the global nanocomposites material features [47, 48]. For example, the interfacial shear strength (ISS) can be increased by creating covalent bonds between the CNTs and the polymers. This will cause an enhancement of the strength and stiffness of the polymer compound through an improved interfacial load transfer, however the persistence of stick-slip will be lost. On the other hand, the onset of the nanocomposites hysteretic response may be facilitated by reducing the strength of the CNT/matrix interface. Consequently, the resulting nanostructured material will show enhanced damping capacity at relatively low strains, without compromising the mechanical properties of the polymer.

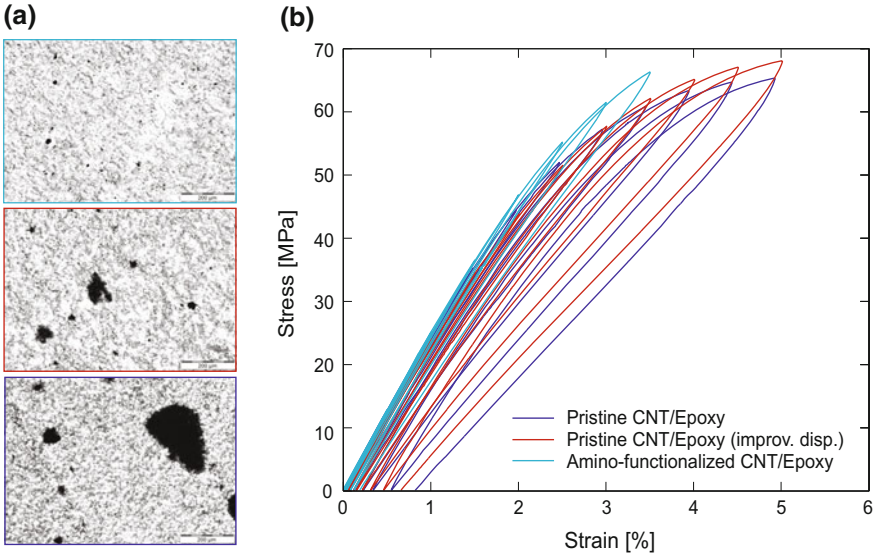

Fig. 13.9 **a** Micrographs of the three nanocomposites denoted by the *blue, red* and *cyan colors*; **b** Cyclic tensile tests on CNT/epoxy nanocomposites obtained via different CNT dispersion treatments: (*blue*) pristine MWNT/epoxy prepared via ultrasonic bath; (*red*) pristine MWNT/epoxy composite prepared via ultrasonic horn; (*cyan*) amino-functionalized MWNT/epoxy composite prepared via ultrasonic horn. The displacement rate was set to 0.2 mm/min and the deformation was increased of 0.5% at each loading cycle until reaching 5%

Strain amplitude-dependent behavior of CNT nanocomposites. After observing the different hysteresis loops via cyclic tensile tests, experimental Dynamic Mechanical Analysis (DMA) tests were carried out to investigate the strain amplitude effect on the damping response of nanocomposites. DMA is a widely used technique by which small deformations or stresses are applied to a sample in a cyclic manner. DMA gives information about the rheology of the material by measuring its viscoelastic properties. The rheology provides a relationship between the inner structure and the macroscopic properties of the nanocomposites, which is the key to the development of new materials. The data collected from the tests may be expressed in terms of storage modulus, loss modulus, or damping. For a given sinusoidal strain time history, the viscoelastic material stress will also vary sinusoidally in time at low strain amplitudes. The stress response will have the same frequency as the input strain but lagging by a phase angle denoted by δ. The phase lag is due to the excess time necessary for molecular motions and relaxations to occur. Dynamic strain and stress are expressed as $\varepsilon = \varepsilon_o \sin(\omega t)$, and $\sigma = \sigma_o \sin(\omega t + \delta)$, respectively, where ω is the angular frequency. The measured stress can be divided into an in-phase component ($\sigma_o \cos\delta$) and an out-of-phase component ($\sigma_o \sin\delta$). Dividing the stress by the strain amplitude, two moduli are derived and defined as E' and E'' for the in-phase and out-of-phase parts, respectively,

$$E' = \frac{\sigma_o}{\varepsilon_o}\cos\delta, \qquad E'' = \frac{\sigma_o}{\varepsilon_o}\sin\delta. \tag{13.3}$$

E' and E'' correspond to the real and imaginary parts of the complex modulus: $E^* = E' + iE''$. The storage modulus E' describes the ability of the material to store potential energy and release it upon deformation. The storage modulus it is associated with the material "stiffness" and is related to the Young modulus. The loss modulus E'' is associated with energy dissipation in the form of heat upon deformation and it is related to "internal friction". The loss modulus is sensitive to different kinds of molecular motions, relaxation processes, transitions, morphology and other structural heterogeneities. Thus, the dynamic properties provide useful information at the molecular level to understand the nanofiller/polymer mechanical behavior. The ratio between the loss modulus and the storage modulus is a measure of the intrinsic damping called loss factor and denoted by $\eta = \tan\delta = E''/E'$. Alternatively, energy concepts can be used. With respect to a steady-state oscillation, η can be described as

$$\eta = \frac{W_D}{2\pi W_E} = \frac{\pi E'' x_o^2}{2\pi(\frac{1}{2}E' x_o^2)} = \frac{E''}{E'}, \tag{13.4}$$

where x_o is the amplitude of the steady-state response, W_D stands for the energy dissipated in a steady-state cycle while W_E represents the stored energy. The loss factor is undoubtedly the most general damping measurement index. The equivalent damping ratio ξ is related to the other damping measures by simple laws: $\eta = \tan\delta = 2\xi$ when damping levels are within $0 < \tan\delta < 0.15$.

DMA tests were carried out using a dynamic thermo-mechanical analyzer (ARES-G2, TA Instruments) to evaluate the variation of (E', E'', η) within selected ranges of the shear strain in torsional mode. The torsional tests provided information about the damping capacity of the nanocomposites, also in terms of the shear stress state that initiated the CNT/matrix stick-slip phenomenon with a significant localization around the contour of the samples cross sections. The strain sweep tests were performed in the strain range from 10^{-4} to 3.5×10^{-2} setting the frequency to 1 Hz, at room temperature. The PC and PBT nanocomposite specimens were rectangular bars with a length of 40 mm and a cross section of $1 \times 9.5\,\text{mm}^2$.

Figure 13.10 shows variations of the damping capacities of CNT/PC and CNT/PBT nanocomposites in a large shear strain range, and provides evidence about the onset of the interfacial stick-slip. Past a critical shear strain value, significant increments of damping ratios are reported for each nanocomposite compared to the neat polymer. These threshold strains identify the onset of the stick-slip phenomenon. More specifically, for low strains, below the threshold strains, the measured damping ratios of nanocomposites are close to the values obtained in the pure matrices and, in some cases, damping is even lower than that exhibited by the polymers. This is because the CNT composites are stiffer that the neat matrices, in which the polymer chains show some mobility and readjustments, even at low strains. However, when the threshold dynamic strain is reached, the energy dissipation in CNT composites is markedly enhanced and it rapidly increases with the dynamic strain [49]. By analyzing the

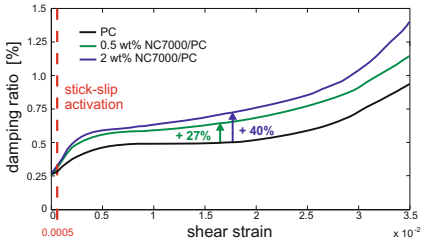

(a) Low aspect ratio MWNT/PC nanocomposites

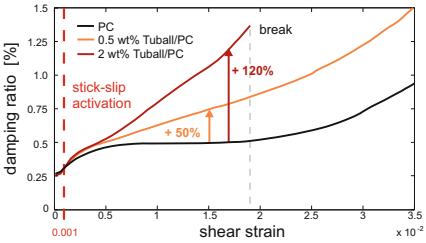

(b) High aspect ratio SWNT/PC nanocomposites

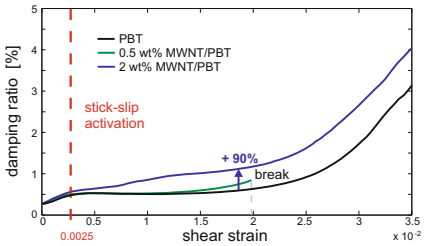

(c) Low aspect ratio MWNT/PBT nanocomposites

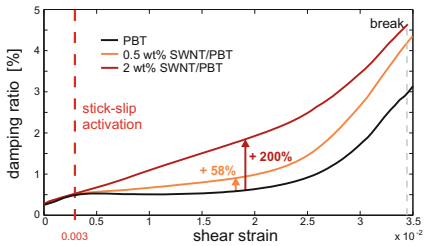

(d) High aspect ratio SWNT/PBT nanocomposites

Fig. 13.10 Damping capacity of the PC and PBT nanocomposites obtained via DMA tests in torsional mode

trend of damping ratio versus shear strain amplitude a threshold strain of 5×10^{-4} is found for MWNT/PC nanocomposite and a threshold strain of 10^{-3} for SWNT/PC nanocomposites, whereas in the CNT/PBT nanocomposites the threshold strain is 2.5×10^{-3} and 3×10^{-3} for MWNT and SWNT nanocomposites, respectively. The threshold strain values provide information about the nanofiller/polymer interactions and suggest that interfaces in SWNT nanocomposites exhibit a better adhesion compared to those of MWNT nanocomposites. The explanation of this behavior is to be found in the nanofiller morphology. TEM analysis reported in [19] highlight the straight and lenghten shape of the SWNTs versus the short and curly shape of the MWNTs. As result, the MWNTs curviness hinders the nanofiller/polymer bonding and make weaker the interfaces in the MWNT nanocomposites.

Besides the dissipation at the interface through stick-slip, additional sources of energy dissipation in nanocomposites at large strain amplitudes could stem from other dissipation phenomena within the matrix. Since it is assumed that the CNTs remain elastic even at large strains, the polymer chains start to relatively slide, especially at the CNTs ends. Furthermore, the way in which the low and high aspect ratio CNTs affect the nanocomposites damping capacity is here highlighted. By adopting high aspect ratio SWNTs, a larger interfacial area is obtained for the stick-slip activation thus providing higher dissipation. When the same CNTs volume fraction is considered, the SWNT/matrix interfacial contact area is estimated to be 5.5 times larger than that available in the MWNT nanocomposites, thus explaining the significantly

higher damping enhancement in all SWNTs nanocomposites. Thus to summarize, at low strain amplitudes, the damping capacity is nearly constant. Above the threshold strain, damping increases with the strain level as a result of the CNT/polymer stick-slip. Moreover, the experimental results show a significant damping improvement by increasing the CNT weight fraction, although the CNT dispersion may become worse. The highest damping enhancement was reported for the 2 wt% SWNT/PBT nanocomposite with 200% increase compared to the neat PBT matrix.

Modeling of hysteresis in CNT nanocomposites. Several analytical/computational models were proposed to describe the nanocomposites nonlinear constitutive behavior. The first efforts aiming at modeling hysteresis in CNT nanocomposites were addressed by Zhou et al. [14], exploiting basic microstructural concepts to describe the interfacial stick-slip in nanocompoites treated as four-phase materials. Li et al. [50] developed a continuum model to describe the interfacial shear stress distribution using a molecular structural mechanics approach and finite element analysis. Interesting friction models for the description of the hysteretic response in CNT nanocomposites were also provided by Huang and Tangpong [51] and by Lin and Lu [52] who modeled the energy dissipation of CNT composites under dynamic loading by considering several crucial aspects, including CNT alignment to optimize the damping response.

Recent advances in the context of smooth hysteresis modeling for nanocomposites were reported in [53, 54] where a multi-scale finite element analysis was carried out to investigate the hysteretic stress-strain behavior of the nanocomposites as well as the influence of the interfacial strength, geometry, volume fraction and elastic properties of the CNTs. In particular, the work of Formica et al. [18, 20] proposed a meso-scale nonlinear incremental constitutive model based on the Eshelby-Mori-Tanaka theory to describe the shear CNT/matrix stick-slip via an inelastic eigenstrain field. The model provided predictions of the hysteretic response in close agreement with experimental results, thus proving its validity.

In the last decade, a huge step forward in modeling the nonlinear response of nanocomposites was taken, also thanks to the progress in nanocomposites manufacturing by which more experimental data were made available to validate the theories. The current goal in analytical modeling is to provide efficient and effective tools able not only to predict the nanocomposites mechanical response, but also to correlate the shape and magnitude of the nanocomposite hysteresis to macro- and micro-structural constitutive parameters. This will enable to design the nanocomposite mechanical properties together with its damping capacity araising from micro-dissipative phenomena, such as the interfacial stick-slip. [20].

13.4 Conclusions

Targeted levels of hysteresis can be achieved in innovative, high-performance structures by either introducing auxiliary point-wise, hysteretic dampers or by leveraging

on the inherent damping capability of nanostructured materials such as carbon nanotube polymer nanocomposites.

This work discussed recent advances in the design of nonlinear rheological devices that make use of dedicated wire ropes which exhibit inter-wire hysteretic frictional damping together with dissipation ensuing from phase transformations in NiTiNOL wires. Moreover, geometric nonlinearities in these devices can be leveraged to conveniently modify the shape of the hysteresis loops thus enabling a wider frequency tuning. The occurrence of friction together with austenitic-martensistic phase tranformations allows to attain energy dissipation over a large displacement range. The possibility to regulate the dissipation level and the effective displacement range makes the rheological device robust for several applications, especially in the field of structural and mechanical vibrations control.

By moving towards a much smaller material scale, desirable hysteresis can be achieved in CNT nanocomposites by taking advantage of the dissipative interfacial stick-slip between the CNTs and the polymer chains. A tailored hysteretic response can be designed through proper choice of the polymer matrix via optimization of the interfacial properties. This can be obtained through an engineering of the interfaces at the micro/nano-scale. Nanoparticle coatings, covalent and non-covalent functionalizations, dispersion treatments and other kinds of surface modifications can be envisioned to selectively modify the interfacial adhesion of the nanofiller with the polymer, and bridge together a variety of structural and nonstructural properties in the same material.

The conducted experimental campaign confirmed that the macroscopic hysteresis can be controlled to within a certain degree in the resulting CNT nanocomposites without compromising the effective stiffness and strength. An increase of 200% in damping capacity was found in randomly oriented 2 wt% SWNT/PBT nanocomposites with a 25% improvement in Young modulus [19]. This opens new perspectives in designing lightweight composites for applications in aerospace and structural engineering as well as in automotive, electronics and biomedical engineering, where also the outstanding electrical and thermal properties of the CNT nanofillers may be conveniently exploited. To mention a few examples, multifunctional nanocomposites—conceived as lightweight, strong, and highly damped composites—can be designed for reconfigurable smart aerostructures or for miniaturized devices, such as microbeam resonators, micropressure sensors and microabsorbers. On the other hand, by exploiting the electrical properties of nanotubes, conductive networks of CNTs may be introduced in polymer based-composite materials to convey thermal gradients and induce a thermomechanical response of viscous polymers via electrical signals. This would allow the design of materials with a thermally activated hysteretic response, which takes advantage of relaxation phenomena in polymer systems. The work here discussed shows that hysteresis can be conceived as a multi-scale feature which can be engineered and delivered through a micro- and nano-structural design of the materials and systems, depending upon the specific needs dictated by new demanding applications.

Acknowledgements Part of the material of this chapter was presented by Walter Lacarbonara in a keynote lecture within the Third International Conference on Structural Nonlinear Dynamics and Diagnosis (CSNDD'2016), Marrakech, Morocco, May 23–25, 2016. This work was partially supported by the European Office of Aerospace Research and Development/Air Force Office of Scientific Research Grant (Grant N. FA9550-14-1-0082 DEF). Dr. Matthew Snyder and Dr. "Les" Lee are gratefully acknowledged for their support and comments.

References

1. Visintin, A.: Differential Models of Hysteresis. Springer, Berlin (1994)
2. Lacarbonara, W.: Nonlinear Structural Mechanics. Theory, Dynamical Phenomena and Modeling. Springer, New York (2013)
3. Vestroni, F., Lacarbonara, W., Carpineto, C.: Hysteretic tuned-mass damper device (TMD) for passive control of mechanical vibrations. Sapienza patent EP 2742254 A1 (2014)
4. Lacarbonara, W., Carboni, B.: Multi-performance hysteretic rheological device. Sapienza pending patent N. PCT/IT2016/000043 (2015)
5. Carboni, B., Lacarbonara, W., Auricchio, F.: Hysteresis of multiconfiguration assemblies of Nitinol and steel strands: experiments and phenomenological identification. J. Eng. Mech. **141**(3), 04014135 (2015)
6. Gibson, R.F.: A review of recent research on mechanics of multifunctional composite materials and structures. Compos. Struct. **92**, 2793–2810 (2010)
7. Li, B., Zhong, W.H.: Review on polymer/graphite nanoplatelet nanocomposites. J. Mater. Sci. **46**, 5595–5614 (2011)
8. Saba, N., Tahir, P.M., Jawaid, M.: A review on potentiality of nano filler/natural fiber filled polymer hybrid composites. Polymers **6**, 2247–2273 (2014)
9. Sun, L., Gibson, R.F., Gordaninejad, F., Suhr, J.: Energy absorption capability of nanocomposites: a review. Compos. Sci. Tech. **69**, 2392–2409 (2009)
10. Koratkar, N.A., Suhr, J., Joshi, A., Kane, R.S., Schadler, L.S., Ajayan, P.M., Bartolucci, S.: Characterizing energy dissipation in single-walled carbon nanotube polycarbonate composites. Appl. Phys. Lett. **87**, 063102 (2005)
11. Suhr J., Koratkar N.A.: Energy dissipation in carbon nanotube composites: a review. J. Mater. Sci. **4**, 4370–4382 (2008)
12. Thostenson, E.T., Ren, Z., Chou, T.W.: Advances in the science and technology of carbon nanotubes and their composites: a review. Compos. Sci. Technol. **61**, 1899–1912 (2001)
13. Rajoria, H., Jalili, N.: Passive vibration damping enhancement using carbon nanotube-epoxy reinforced composites. Compos. Sci. Technol. **65**, 2079–2093 (2005)
14. Zhou, X., Shin, E., Wang, K.W., Bakis, C.E.: Interfacial damping characteristics of carbon nanotube-based composites. Compos. Sci. Technol. **64**, 2425–2437 (2004)
15. Formica, G., Lacarbonara, W., Alessi, R.: Vibrations of carbon nanotube-reinforced composites. J. Sound Vib. **329**, 1875–1889 (2010)
16. Khan, S.U., Li, C.Y., Siddiqui, N.A., Kim, J.K.: Vibration damping characteristics of carbon fiber-reinforced composites containing multi-walled carbon nanotubes. Compos. Sci. Technol. **71**, 1486–1494 (2011)
17. Alnefaie, K.A., Aldousari, S.M., Khashaba, U.A.: New development of self-damping MWCNT composites. Compos. A **52**, 1–11 (2013)
18. Formica, G., Taló, M., Lacarbonara, W.: Nonlinear modeling of carbon nanotube composites dissipation due to interfacial stick-slip. Int. J. Plast **53**, 148–163 (2014)
19. Taló M., Krause B., Pionteck J., Lanzara G., Lacarbonara W.: An updated micromechanical model based on morphological characterization of carbon nanotube nanocomposites. Compos. Part B: Eng. **115**, 70–78 (2016)

20. Formica, G., Lacarbonara, W.: Three-dimensional modeling of interfacial stick-slip in carbon nanotube nanocomposites. Int. J. Plast **53**, 205–218 (2017)
21. Cardou, A., Jolicoeur, C.: Mechanical models of helical strands. Appl. Mech. Rev. **50**(1), 1–14 (1997)
22. Carboni, B., Lacarbonara, W.: Nonlinear dynamic characterization of a new hysteretic device: experiments and computations. Nonlinear Dyn. **83**(1–2), 23–39 (2016)
23. ABAQUS 6.7: Users manual. Inc. and Dassault Systèmes (2007)
24. Carboni, B., Lacarbonara, W.: Nonlinear vibration absorber with pinched hysteresis: theory and experiments. J. Eng. Mech. **142**(5), 04016023 (2016)
25. Storn, R., Price, K.: Differential evolution-a simple and efficient heuristic for global optimization over continuous space. J. Global Optim. **11**(4), 341–359 (1997)
26. Brewick, P.T., Masri, S.F., Carboni, B., Lacarbonara, W.: Data-based nonlinear identification and constitutive modeling of hysteresis in NiTiNOL and steel strands. J. Eng. Mech. **142**, 04016107 (2016)
27. Bouc, R.: Forced vibration of mechanical systems with hysteresis. In: Proceedings of the Fourth Conference on Non-linear Oscillation, Prague, Czechoslovakia (1967)
28. Wen, Y.K.: Method for random vibration of hysteretic systems. J. Eng. Mech. **102**(2), 249–263 (1967)
29. Carboni, B., Lacarbonara, W., Mancini, C.: Hysteretic beam model for steel wire ropes hysteresis identification. Struct. Nonlinear Dyn. Diagn. 261–282 (2015)
30. Den Hartog, J.P., Ormondroyd, J.: Theory of the dynamic vibration absorber. J. Appl. Mech. **50**(4), 11–22 (1928)
31. Den Hartog, J.P.: Mechanical Vibrations. Dover Publications (2013)
32. Randall, S.E., Halsted, D.M., Taylor, D.L.: Optimum vibration absorbers for linear damped systems. J. Mech. Des. **103**(4), 908–913 (1981)
33. Warburton, G.B.: Optimum absorber parameters for various combinations of response and excitation parameters. Earthq. Eng. Struct. Dyn. **10**(3), 381–401 (1982)
34. Tsai, H.C., Lin, G.C.: Optimum tuned-mass dampers for minimizing steady-state response of support-excited and damped systems. Earthq. Eng. Struct. Dyn. **22**(11), 957–973 (1993)
35. Ioi, T., Ikeda, K.: On the dynamic vibration damped absorber of the vibration system. Bull. JSME **21**(151), 64–71 (1978)
36. Lanzara, G.: Realization and analysis of carbon nanotube carpet microstructures, PhD Thesis in Structural Engineering, Sapienza University of Rome (2006)
37. Lanzara, G.: Carbon nanotube micropillars for strain sensing, Paper No. DETC2015-47783, ASME 2015 International Design Engineering Technical Conferences and Computers and Information in Engineering Conference, Boston; 2–5 August 2015, pp. V004T09A027, 7 pages (2015)
38. Lanzara, G., Chang, F.K.: Design and characterization of a carbon-nanotube-reinforced adhesive coating for piezoelectric ceramic discs. Smart Mater. Struct. **18** (2009)
39. Johnston, I.D., McCluskey, D.K., Tan, C.K.L., Tracey, M.C.: Mechanical characterization of bulk Sylgard 184 for microfluidics and microengineering. J. Micromech. Microeng. **24**(7), 035017 (2014)
40. Kim, T.K., Kim, J.K., Jeong, O.C.: Measurement of nonlinear mechanical properties of PDMS elastomer. Microelectron. Eng. **88**, 1982–1985 (2011)
41. Liu, M., Sun, J., Sun, Y., Bock, C., Chen, Q.: Thickness-dependent mechanical properties of polydimethylsiloxane membranes. J. Micromech. Microeng. **19**, 035028 (2009)
42. Samali, B., Attard, M.M., Song, C.: From Materials to Structures: Advancement Through Innovation. CRC Press, Boca Raton (2012)
43. Ogasawara, T., Tsuda, T., Takeda, N.: Stress-strain behavior of multi-walled carbon nanotube/PEEK composites. Compos. Sci. Technol. **71**, 73–78 (2011)
44. Suhr, J., Koratkar, N.A., Keblinski, P., Ajayan, P.: Viscoelasticity in carbon nanotube composites. Nat. Mater. **4**, 134–137 (2005)
45. Dwaikat, M.M.S., Spitas, C., Spitas, V.: A model for elastic hysteresis of unidirectional fibrous nano composites incorporating stick-slip. Mater. Sci. Eng., A **530**, 349–356 (2011)

46. Ma, P.C., Siddiqui, N.A., Marom, G., Kim, J.K.: Dispersion and functionalization of carbon nanotubes for polymer-based nanocomposites: a review. Compos. A **41**, 1345–1367 (2010)
47. Bose, S., Khare, R.A., Moldenaers, P.: Assessing the strengths and weaknesses of various types of pre-treatments of carbon nanotubes on the properties of polymer/carbon nanotubes composites: a critical review. Polymer **51**, 975–993 (2010)
48. Rohini, R., Katti, P., Bose, S.: Tailoring the interface in graphene/thermoset polymer composites: a critical review. Polymer **70**, 17–34 (2015)
49. Gardea, F., Glaz, B., Riddick, J., Lagoudas, D.C., Naraghi, M.: Energy dissipation due to interfacial slip in nanocomposites reinforced with aligned carbon nanotubes. ACS Appl. Mater. Interfaces **7**, 9725–9735 (2015)
50. Li, C., Chou, T.W.: Multiscale modeling of carbon nanotube reinforced polymer composites. J. Nanosci. Nanotechnol. **3**, 423–430 (2003)
51. Huang, Y., Tangpong, X.W.: A distributed friction model for energy dissipation in carbon nanotube-based composites. Commun. Nonlinear Sci. Numer. Simul. **15**, 4171–4180 (2010)
52. Lin, R.M., Lu, C.: Modeling of interfacial friction damping of carbon nanotube-based nanocomposites. Mech. Syst. Signal Process. **24**, 2996–3012 (2010)
53. Spitas, V., Spitas, C., Michelis, P.: Modeling of the elastic damping response of a carbon nanotube-polymer nanocomposite in the stress-strain domain using an elastic energy release approach based on stick-slip. Mech. Adv. Mater. Struct. **20**, 791–800 (2013)
54. Triantafyllou, S.P., Chatzi, E.N.: A hysteretic multiscale formulation for nonlinear dynamic analysis of composite materials. Comput. Mech. **54**, 763–787 (2014)